Subseasonal Temporal Clustering of Extreme Precipitation in the Northern Hemisphere: Regionalization and Physical Drivers

ALEXANDRE TUEL[a,b] AND OLIVIA MARTIUS[a,b,c]

[a] *Institute of Geography, University of Bern, Bern, Switzerland*
[b] *Oeschger Centre for Climate Change Research, University of Bern, Bern, Switzerland*
[c] *Mobiliar Laboratory for Natural Risks, University of Bern, Bern, Switzerland*

(Manuscript received 26 August 2021, in final form 2 February 2022)

ABSTRACT: Temporal clustering of extreme precipitation (TCEP) at subseasonal time scales often results in major impacts on humans and ecosystems. Assessment and mitigation of the risk of such events requires characterization of their weather/climate drivers and their spatial dependence. Here, we introduce a regionalization method that identifies coherent regions in which the likelihood of subseasonal TCEP exhibits similar dependence to large-scale dynamics. We apply this method to each season in the Northern Hemisphere using ERA5 reanalysis data. The analysis yields spatially coherent regions, primarily at high latitudes and along the eastern margins of ocean basins. We analyze the large-scale and synoptic conditions associated with TCEP in several of the identified regions, in light of three key ingredients: lifting, moisture availability, and persistence in synoptic conditions. We find that TCEP is often directly related to distinct cyclone and blocking frequency anomalies and upper-level wave patterns. Blocking and associated Rossby wave breaking are particularly relevant at high latitudes and midlatitudes. At upper levels, meridional wave patterns dominate; however, in western Europe and parts of North America, TCEP is sometimes associated with zonally extended wave patterns. The flow features associated with TCEP in the eastern Pacific and eastern Atlantic Oceans exhibit similarities. For some regions, moisture flux anomalies are present during clustering episodes whereas in others forced lifting alone is sufficient to trigger heavy precipitation. Our results provide new information on the dynamics and spatial dependence of TCEP that may be relevant for the subseasonal prediction of clustering episodes.

KEYWORDS: Extreme events; Precipitation; Hydrometeorology; Regression analysis; Statistical techniques; Clustering

1. Introduction

The impacts of extreme weather events are often largest when they occur in close succession, in which case one talks of temporal clustering (Zscheischler et al. 2020). Temporal clustering of heavy precipitation can lead to flooding with important implications for the insurance industry and others (Vitolo et al. 2009). Recent devastating floods in Pakistan (Martius et al. 2013), in the United Kingdom (Blackburn et al. 2008; Priestley et al. 2017), in California (Moore et al. 2020), and in southern Switzerland (Barton et al. 2016) have all been linked to recurrent extreme precipitation events over two to six weeks. Characterizing and understanding the tendency of precipitation extremes to cluster in time and space is thus crucial to assessing and mitigating associated risks and improving our ability to forecast temporal clustering at subseasonal time scales.

Our knowledge about the drivers of subseasonal temporal clustering of extreme precipitation (TCEP) stems mainly from case studies from across the world [e.g., western Europe (Blackburn et al. 2008; Huntingford et al. 2014; Davies 2015; Barton et al. 2016; Priestley et al. 2017), southwestern Asia (Martius et al. 2013), or California (Moore et al. 2020)]. More systematic approaches involve various statistical and physical frameworks. Some physical studies have analyzed regional-scale temporal clustering of weather systems generally associated with extreme precipitation, including North Atlantic cyclones (Mailier et al. 2006; Vitolo et al. 2009; Pinto et al. 2013; Dacre and Pinto 2020) and atmospheric rivers in western North America (Payne and Magnusdottir 2014). Statistical analyses by Barton et al. (2016) and Tuel and Martius (2021) both used Ripley's K function to detect statistically significant TCEP in southern Switzerland and globally respectively. Villarini et al. (2011) implemented Poisson regressions on annual extreme precipitation event counts across the American Midwest to identify TCEP and link it to large-scale modes of climate variability. Similarly, Yang and Villarini (2019) used Cox regression to link TCEP in Europe to variability in the Arctic Oscillation and North Atlantic Oscillation.

Case studies provide insights into the mechanisms conducive to TCEP, but do not allow generalization. Regression approaches with large-scale teleconnection indices as covariates can highlight their influence on TCEP (e.g., Villarini et al. 2011). However, these indices may not represent the most relevant

Denotes content that is immediately available upon publication as open access.

Supplemental information related to this paper is available at the Journals Online website: https://doi.org/10.1175/JCLI-D-21-0562.s1.

Corresponding author: Alexandre Tuel, alexandre.tuel@giub.unibe.ch

DOI: 10.1175/JCLI-D-21-0562.1

atmospheric configurations, and they lack a direct connection to physical processes.

To address these limitations and explore the issue of spatial dependence, we propose a simple statistical method that highlights the processes associated with TCEP and identifies regions where these processes are similar. Our proposed method uses *k*-means clustering (hereinafter referred to as *k*-means regionalization) of the coefficients of Poisson regression models for extreme event counts. Our covariates are principal component time series of the 500-hPa geopotential field. We apply the method to the Northern Hemisphere and to each season. This hemispheric scope goes beyond previous studies.

We also analyze atmospheric conditions during clustering periods. TCEP requires three main ingredients (Doswell et al. 1996). The first two are common to all extreme precipitation events: strong lifting and sufficient moisture. The third, persistence of conditions favorable to extreme precipitation, is specific to TCEP events. Persistence of specific weather conditions can mean that they either last for a long time or occur several times in a subseasonal time window. Various processes may provide the lifting: upper-level divergence, warm conveyor belts (e.g., Pfahl et al. 2014), fronts (e.g., Catto and Pfahl 2013), convective instability (Lamb 2001), or the interaction of the flow with orography (e.g., Smith and Barstad 2004). Moisture availability typically results from high vertically integrated water vapor transport (IVT), often following intense surface evaporation (e.g., Winschall et al. 2014; Piaget et al. 2015). High IVT in the midlatitudes mostly originates from the tropics and subtropics, where moisture is more abundant (Gimeno et al. 2010; Nieto et al. 2019). Temporal persistence in these processes can therefore arise from various factors, like the repeated occurrence of cyclones (Dacre and Pinto 2020) and upper-level disturbances, for instance recurrent Rossby waves (Röthlisberger et al. 2019; Ali et al. 2021) and Rossby wave breaking (de Vries 2021). Temporal persistence may in addition result from persistent atmospheric circulation, linked to quasi-stationary waves (Kornhuber et al. 2017) and long-lived or recurrent blocks. Sea surface temperature anomalies that persist for weeks or even months can also play an important role by modulating atmospheric circulation, surface evaporation, and atmospheric stability.

Consequently, we seek to identify the processes responsible for lifting, moisture availability, and persistence. Our proxies for lifting are upper-level flow and cyclone frequency. Moisture availability is assessed with IVT and total column water. We investigate possible drivers of persistence by looking at sea surface temperatures, blocking frequency, 200-hPa wind velocity to characterize the position of the midlatitude jet, and the dynamical tropopause to detect Rossby wave breaking (RWB). Our results provide insights into the spatial structure of TCEP and its dependence on atmospheric dynamics.

2. Data and methods

a. Data

This study uses data from the ERA5 reanalysis (Hersbach et al. 2020) over the Northern Hemisphere (0°–80°N) for 1979–2019 at 1° × 1° spatial resolution and 6-hourly temporal resolution. The data include daily precipitation, 500-hPa geopotential (Z500), 200-hPa wind velocity (W200), water vapor transport integrated between 1000 and 100 hPa (IVT), total column water (TCW), and sea surface temperature (SST). From ERA5 model-level wind, temperature, and pressure, we calculate Ertel potential vorticity (PV) interpolated to isentropic levels between 320 and 340 K. We use different isentropic levels for PV analyses for each of the four seasons, following Röthlisberger et al. (2018): 320 K in winter [December–February (DJF)], 325 K in spring [March–May (MAM)], 340 K in summer [June–August (JJA)], and 330 K in autumn [September–November (SON)]. We use the binary blocking and cyclone detection indices computed by Rohrer et al. (2020) adapted from the original indices proposed by Schwierz et al. (2004) (blocks) and Wernli and Schwierz (2006) (cyclones). Blocks are identified as regions of persistent negative anomalies of 500–150-hPa vertically integrated PV, and cyclones as closed sea level pressure contours lasting at least 4 days.

The use of ERA5 daily precipitation is constrained by the lack of a global and consistent gridded record of daily precipitation covering such a long period of time. Satellite- and station-based datasets are more limited in time (typically from the late 1990s only) and/or in space (no global coverage). They do not perfectly represent extreme precipitation statistics either. Although precipitation in ERA5 is not assimilated, it compares well to satellite- and station-based precipitation datasets, from the tropics to the midlatitudes, for timing (Rivoire et al. 2021) and temporal clustering (Tuel and Martius 2021) of precipitation extremes. Choosing to work with ERA5 precipitation also ensures the dynamical consistency with the large-scale dynamics.

b. Methods

Our method involves three steps: first, we implement a regression model at each grid point to identify Z500 patterns associated with TCEP events. Next, a *k*-means regionalization is applied to the regression coefficients to identify spatial regions in which the dependence to Z500 variability is roughly homogeneous. Finally, we interpret the results physically by looking at anomalies of atmospheric variables and SSTs when TCEP events occur in selected regions. The method is applied to each season (DJF, MAM, JJA and SON) separately. A summary of the method appears in Fig. 1.

1) Statistical modeling of temporally compounding precipitation extremes

Precipitation extremes are defined at each grid point as days when daily precipitation exceeds its 99th all-days percentile for the corresponding month. Taking monthly percentiles removes the seasonality in precipitation magnitude to concentrate on subseasonal time scales (Tuel and Martius 2021) and ensures a constant rate of extreme precipitation occurrence throughout the year. Time series of precipitation extremes typically exhibit short-term (2–3 days) dependence due to the persistence of weather systems. This dependence is removed through a standard runs declustering method (Coles 2001) in which events separated by less than 2 days are assigned to the same extreme precipitation event. Extreme events counts $n_t \in \mathrm{N}$

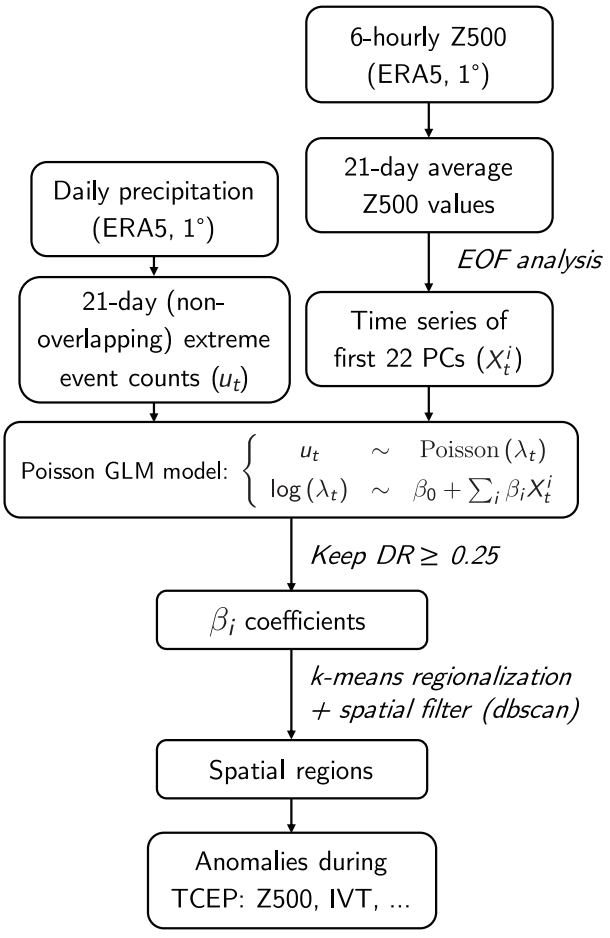

FIG. 1. Summary of the method adopted in this study (see the main text for an explanation of the acronyms).

are computed over successive, nonoverlapping 3-week windows (indexed by t) for 1979–2019. A 3-week window is well suited to quantifying clustering at subseasonal time scales (Kopp et al. 2021; Tuel and Martius 2021). Each window is then assigned to the season with which it overlaps the most. In each season, grid points where 99th daily precipitation percentiles are less than 1 mm for at least 2 months are excluded from the analysis.

We model 3-week extreme event counts n_t, for each grid point and season, with Poisson generalized linear models (GLMs). Note that n_t is assumed to follow a Poisson distribution with rate of occurrence λ_t that depends on covariates X_t^i as follows:

$$\begin{cases} n_t \sim \text{Poisson}(\lambda_t) \\ \log(\lambda_t) = \beta_0 + \sum_{i=1}^{22} \beta_i X_t^i \end{cases}. \tag{1}$$

For covariates X_t^i we consider the principal component (PC) time series of Northern Hemisphere Z500 averaged over the same 3-week windows used to define n_t. We use the first 22 PCs, which account for at least 90% of total variance in each season. The Z500 data are weighted by latitude. The number of possible covariates is rather high, so the Poisson GLM fit is performed with least absolute shrinkage and selection operator (LASSO) regression, using the R package "glmnet" (Friedman et al. 2010). Goodness of fit is then assessed with the model deviance ratio (DR), defined as

$$\text{DR} = 1 - \frac{D}{D_0}, \tag{2}$$

where D is the model deviance, equal to $2[\ell_s - \ell(\boldsymbol{\beta})]$, where ℓ_s is the log-likelihood of the saturated model (with one free parameter per observation) and $\ell(\boldsymbol{\beta})$ is the log-likelihood of the fitted model. The term D_0 is the deviance of the null model, in which $\lambda_t = \lambda_0$. DR thus measures the improvement of the model from the null baseline; DR close to 0 means that the model performs hardly better than the null one, whereas DR close to 1 implies an almost-perfect model. The validity of the Poisson distribution assumption for n_t is assessed with a χ^2 test on model deviance D. Under the null hypothesis that the assumed Poisson model is correct, D follows a χ^2 distribution with n degrees of freedom, where n equals the number of observations minus the number of model parameters.

2) K-MEANS REGIONALIZATION

DR indicates how relevant large-scale dynamics are in explaining variability in n_t. Consequently, we first retain only grid points for which DR $\geq$ 0.25 to select locations where large-scale dynamics exert a strong control on extreme event counts. This choice is subjective; it is high enough to ensure reasonable goodness of fit, but it excludes a large fraction of points where large-scale dynamics may still be relevant but their influence is weak or poorly modeled with our covariates.

We then implement a k-means regionalization algorithm on the vectors of coefficients $\boldsymbol{\beta} \in \mathbb{R}^{22}$. Given a number of regions and initial region centroids, the k-means algorithm proceeds iteratively by reassigning each point to the region with the nearest centroid (using the Euclidean distance). The algorithm stops when no more reassignments are possible. Following Fränti and Sieranoja (2019), we initialize centroids using the farthest point heuristic (maxmin; the first centroid is randomly chosen, and subsequent centroids are chosen as far from the previous centroids as possible). Because k-means regionalization requires the number of regions as input, we first calculate the average silhouette coefficient over all points for all region numbers between 3 and 40, from 100 realizations of the k-means algorithm for each region number. The silhouette coefficient compares the average intracluster and intercluster distance; the higher it is, the more clearly distinguished the clusters are. We then choose the optimal region number k^* that maximizes the silhouette coefficient. Then, we select the realization with the lowest total sum of squares (which provides the best partition into k^* regions). Each region is then screened for points far away from all others in the region. This step is useful because the DR maps can be very noisy (see Fig. S2 in the online supplemental material). We use the "dbscan" algorithm (Ester et al. 1996) so that each region point has at least 10 neighboring points in the same region within

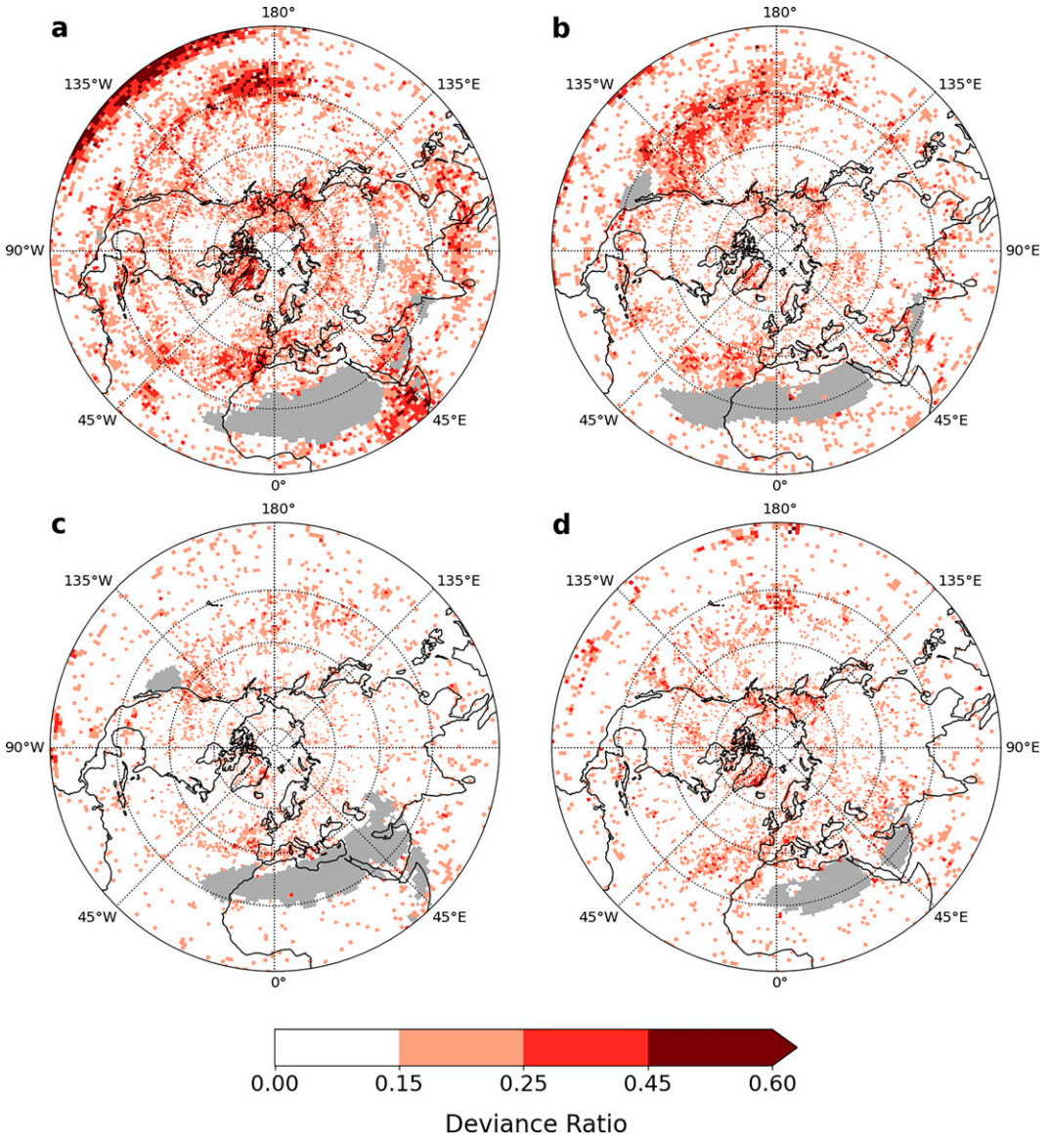

FIG. 2. Deviance ratio in the Poisson GLM model for (a) DJF, (b) MAM, (c) JJA, and (d) SON. Areas where the seasonal 99th percentiles of daily accumulated precipitation are less than 1mm are shown in gray.

500 km. These values were chosen to eliminate outlying points without affecting the regions' spatial coherence.

3) SYNOPTIC-SCALE CONDITIONS DURING TCEP EVENTS

For each region $\mathcal{S}$ thus obtained, we consider that TCEP occurs in $\mathcal{S}$ during a given 3-week period when at least 10% of region points experience more than 1 extreme precipitation event. Thus, for each region and season, we obtain a given number of TCEP periods M (typically 6–15). We then calculate anomalies of 3-week mean Z500, IVT, TCW, W200, blocking and cyclone frequency indices, PV, and SST averaged over the M TCEP periods. To assess the statistical significance of these anomalies, we calculate at each grid point their rank among a sample of 1000 anomalies obtained from randomly generated sets of M periods belonging to the same season. This rank determines a p value on which we implement a two-tailed t test with a false discovery rate (FDR) (Wilks 2016) of 10%.

3. Results

We first discuss the goodness of fit of the Poisson GLM before presenting the results of the regionalization algorithm. Circulation anomalies associated with several regions are then described.

a. Poisson GLM

Two main results stand out from the analysis of the spatial distribution of DR by season (Fig. 2). First, DR exhibits strong

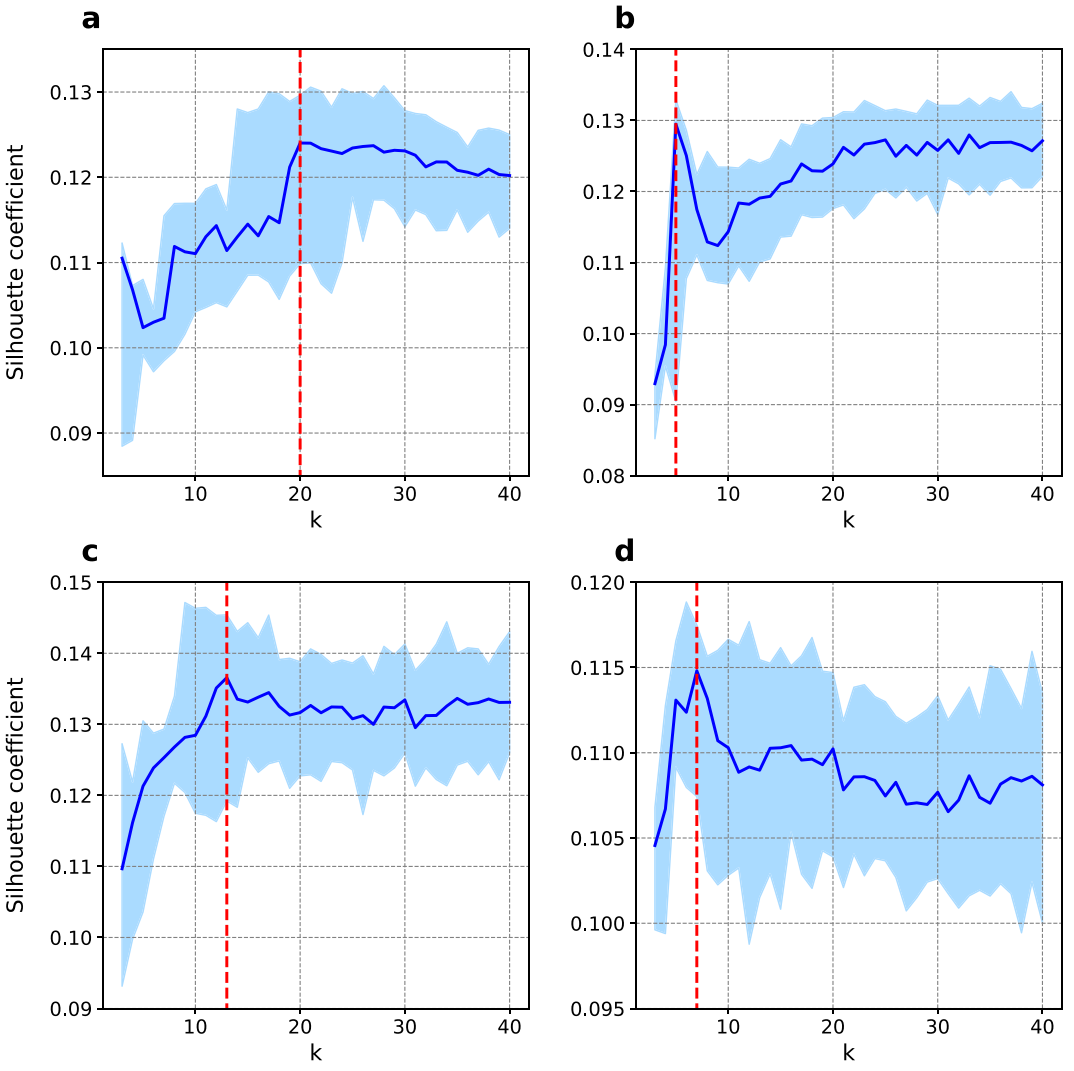

FIG. 3. Silhouette coefficient as a function of region number k in (a) DJF, (b) MAM, (c) JJA, and (d) SON for an ensemble of 100 k-means regionalization results. Shown are the ensemble mean (solid blue line) and 95% range (blue shading). Red vertical lines indicate the number of regions for which the ensemble mean of the silhouette coefficient is maximal.

spatial discrepancies. DR maps are noisy, but spatially coherent regions with high DR values (≥0.3) clearly emerge in the high latitudes (≥60°N), over the eastern half of ocean basins (10°–40°N in the North Pacific Ocean and 20°–45°N in the North Atlantic Ocean) and, to a lesser extent, in some equatorial regions. Locally, smaller coherent regions with medium (0.15–0.3) DR values exist: the continental United States and Mexico, Russia, and the central subtropical Atlantic in DJF and southwestern Asia in SON. The rest of the Northern Hemisphere generally shows no to little model skill. Note that the Poisson assumption is overall valid, especially outside the tropics, with the exception of the equatorial Pacific in JJA and SON (Fig. S1 in the online supplemental material). In all regions of high DR, extreme event counts can be assumed to follow Poisson distributions. Second, the seasonality in model performance is obvious: DR values are largest in DJF (hemispheric-wide median DR 0.1) and lowest in JJA (median 0.02). In DJF, 18% of grid points have a DR value above 0.25; in MAM, 8% do; in JJA, 4% do; and in SON, 6% do. Regions over the subtropical-to-midlatitude ocean basins generally show high model skill across the year, with some indications of a poleward shift in JJA relative to DJF (Figs. 2a,c). High-DR areas over the equatorial Pacific, East Africa, and the Maritime Continent are prominent in DJF but absent in other seasons. Similarly, model skill is very weak in JJA northward of 60°N, where DR values in other seasons are very large.

b. *Regionalization results*

We begin by determining optimal region numbers for each of the four seasons. Average silhouette coefficients exhibit peaks at $k^* = 20$ (DJF), $k^* = 6$ (MAM), $k^* = 13$ (JJA), and $k^* = 8$ (SON) (Fig. 3). The peak for SON is very distinct

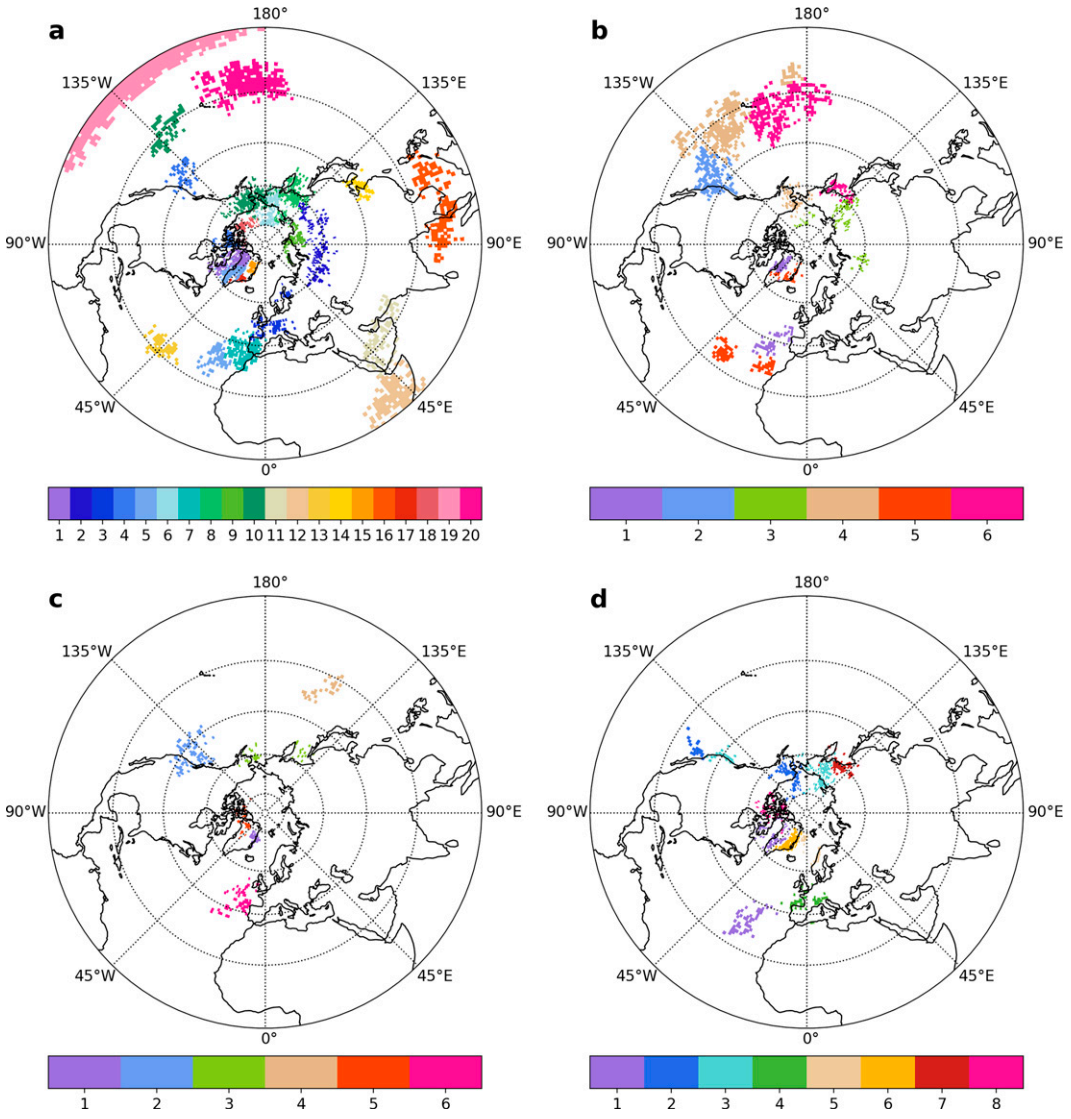

FIG. 4. Regionalization results for (a) DJF, (b) MAM, (c) JJA, and (d) SON.

(Fig. 3d), whereas in DJF and JJA the average silhouette coefficient values tend to stagnate after reaching their peaks (Figs. 3a,c). In MAM, silhouette coefficients drop after the peak but slowly increase again with the number of regions and reach a plateau beyond 20 regions (Fig. 3b). For any silhouette coefficient, without additional a priori knowledge, we select the partition with the fewest regions and thus retain the k^* values given above for our final partition.

Regionalization results are shown in Fig. 4. For all seasons except JJA, the final number of regions is equal to k^*; for JJA, however, many $k^* = 13$ regions do not pass the test for spatial coherence: only six regions are retained. Overall, regions all exhibit strong spatial coherence, even in the unfiltered data (Fig. S1 in the online supplemental material). Consistent with the distribution of DR values (Fig. 2), regions are concentrated over the eastern halves of the two ocean basins and at high latitudes. However, several regions are found over continents (Fig. 4): western/northern Europe in DJF (regions 3 and 7) and SON (region 4); several regions in Siberia and northeastern Asia in all seasons except JJA; and, in DJF, northeastern China and the Korean Peninsula (region 14), southwestern Asia (region 11), and East Africa (region 12). Most regions consist of one group of closely located points, except for some regions over the North Pacific and Atlantic Oceans, which include both high-latitude and subtropical or midlatitude regions. In DJF, for instance, region 5 includes points located off the northwestern African coast, and the southwestern quadrant of Greenland (Fig. 4a). There also appears to be some continuity in region structure across seasons, for instance between regions 1 (SON), 5 (DJF), and 1 (MAM) in the North Atlantic, or regions 4 (DJF), 2 (MAM), and 2 (JJA) over western North America. Regions 10 (DJF) and 4 (MAM) are also very similar.

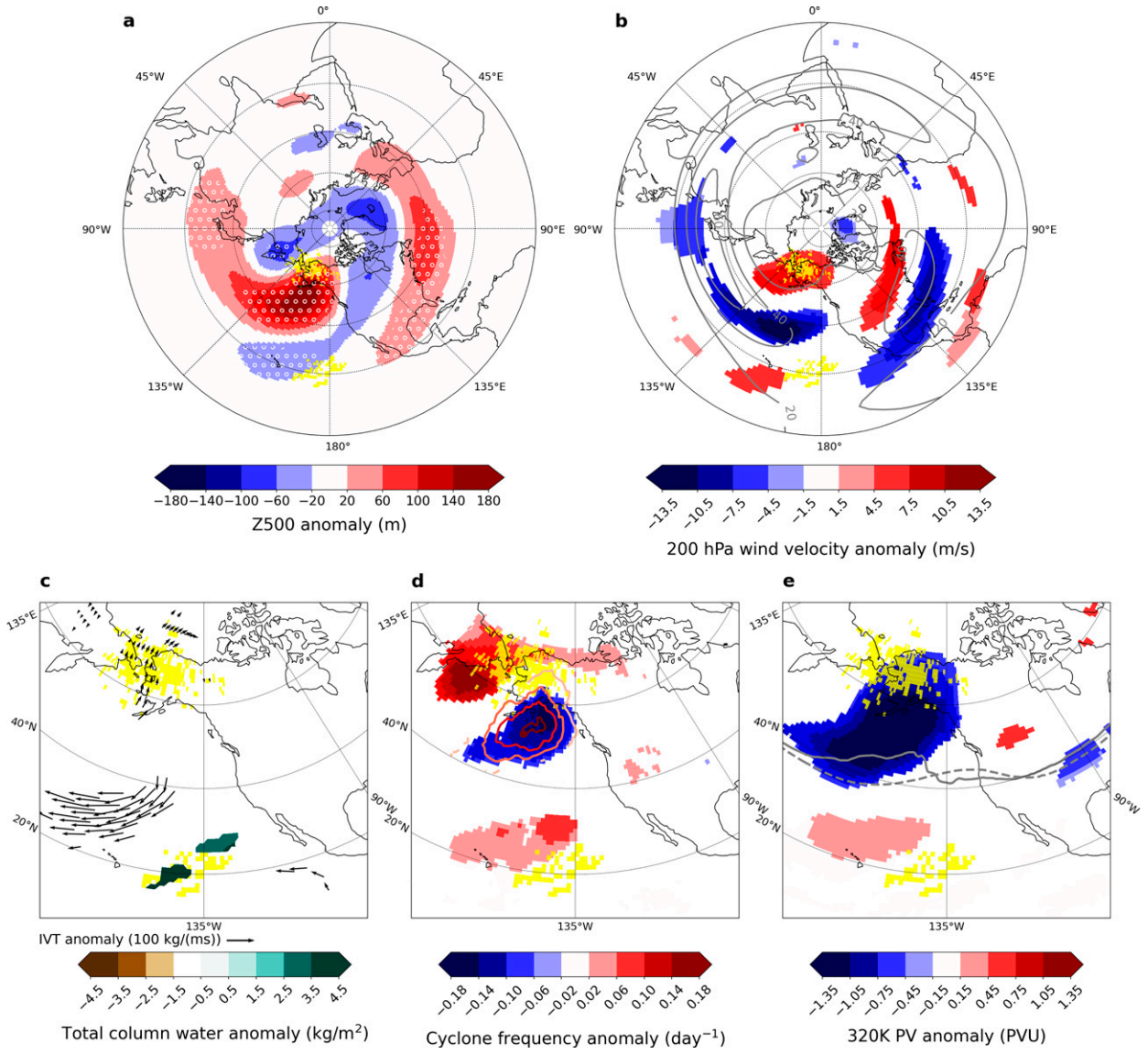

FIG. 5. Large-scale conditions associated with temporally compounding precipitation extremes for DJF region 10 (Fig. 4a), showing anomalies during 3-week periods in DJF when more than 10% of grid points belonging to the region experience two or more precipitation extremes: (a) Z500, (b) W200, (c) TCW (shaded) and IVT (arrows), (d) cyclone frequency (shaded) and blocking frequency (contour lines), and (e) PV anomalies (color shading) and event composite 2-PVU contour (solid line) and climatological 2-PVU contour (dashed line) on the 320-K isentropic surface. In (d), the lowest contour line (light red) corresponds to 0.05, and contours increase by 0.05 afterward. In (b)–(e), only anomalies significant to the 10% level according to the FDR test (see the main text) are shown. In (a), the significance of the anomalies is indicated by white stippling. In all panels, the location of the region is indicated by the yellow shading.

c. *Circulation anomalies associated with TCEP*

The analysis of large-scale atmospheric conditions during TCEP events is organized geographically; regions in the North Pacific, North Atlantic, and Europe are discussed in turn. We focus on a subset of representative regions for brevity. We refer to regions using their numbers on Fig. 4 and for each we show the associated (i) Z500 anomalies, (ii) W200 anomalies against the seasonal climatology, (iii) IVT and TCW anomalies, (iv) anomalies of cyclone and blocking frequencies, and (v) PV anomalies on the isentropic level corresponding to the season of analysis, and 2-PVU (1 PVU $\equiv 1.0 \times 10^{-6}$ m^2 s^{-1} K kg^{-1}) contour (dynamical tropopause) location against its seasonal mean. SST anomalies are only mentioned when statistically significant. The word "significant" refers exclusively to statistical significance as determined in section 3.

1) NORTH PACIFIC

TCEP in regions over Alaska and the subtropical northeastern Pacific (region 10 in DJF, region 4 in MAM, and region 2 in SON; Figs. 4 and 5, see also Figs. S3 and S4 in the online

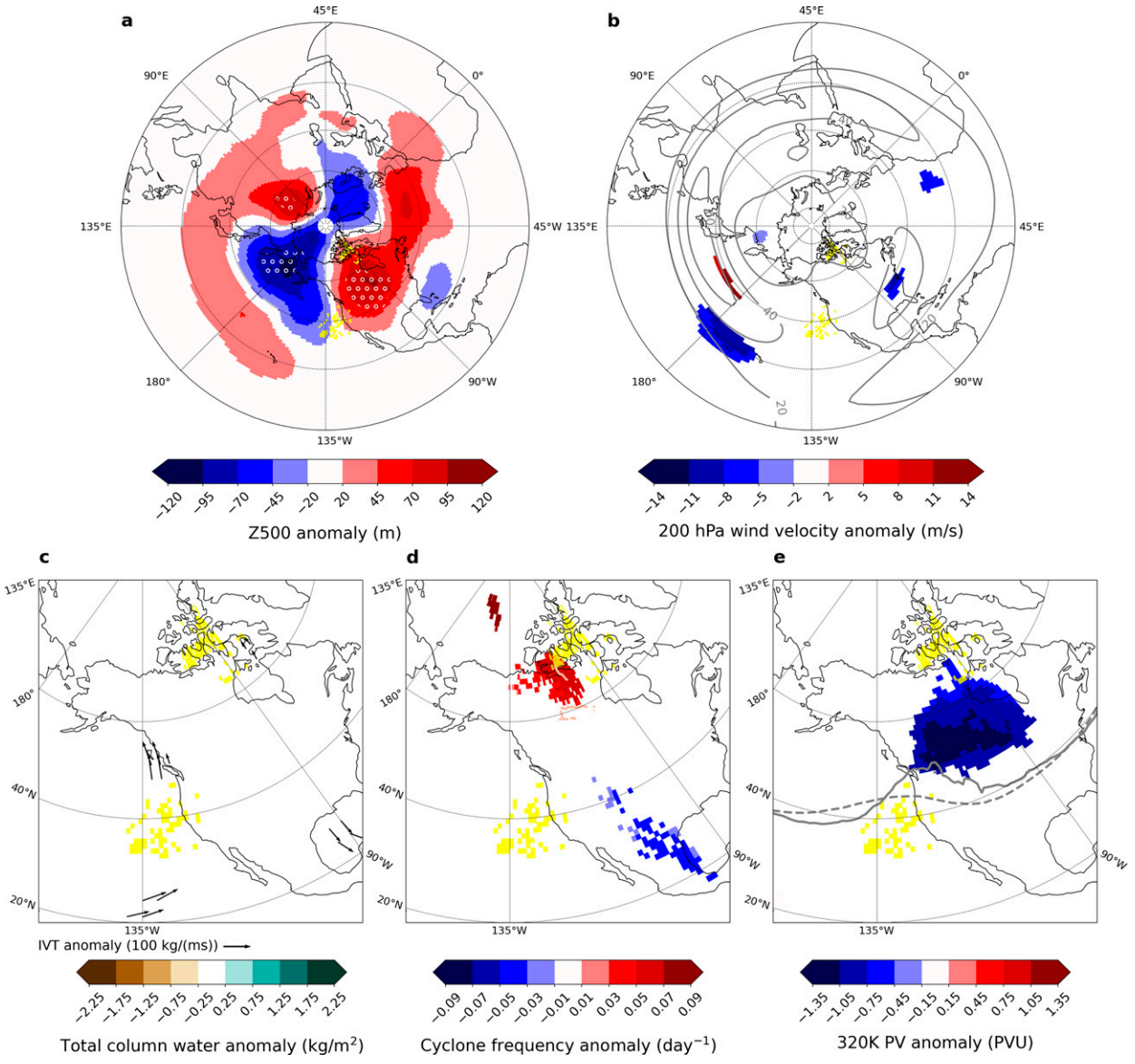

FIG. 6. As in Fig. 5, but for DJF region 4.

supplemental material) is consistently associated with a strong ridge over the Gulf of Alaska and troughs to the south and east (Figs. 5a), and blocking, reduced cyclonic activity in the blocked area, and enhanced cyclonic activity upstream and downstream of the block (Fig. 5d). TCEP mainly occurs on the warm (southeast) side of areas with positive cyclone anomalies. Warm conveyor belts are therefore potentially responsible for the lifting of air masses. Moisture availability over Alaska is linked to anomalous southerly IVT, but to the south we find no significant IVT signal but positive TCW anomalies (Fig. 5c). The jet at 200 hPa is weaker and broader in its exit region over the eastern North Pacific (Fig. 5b). Strong negative PV anomalies (>1 PVU) are found above the blocked areas, along with positive anomalies downstream to the southeast, which overlap the areas of enhanced cyclonic activity (Fig. 5e).

Some notable differences can be found between seasons. The location of W200 anomalies over the eastern North Pacific shifts in latitude following the jet position. Additionally, blocking anomalies south of Alaska and the trough over Canada are much stronger in DJF and MAM than in SON (Fig. S4a). In DJF, significant circulation anomalies also extend into the North Atlantic, where they project onto a positive North Atlantic Oscillation (NAO) phase (Figs. 5a,b). In MAM and SON, moisture availability in the southern half of the region appears directly related to anomalous southwesterly (MAM) and southerly (SON) IVT in the subtropical Pacific (Figs. S3c and S4c).

Regions along the western coast of the United States (region 4 in DJF and region 2 in MAM, JJA, and SON; Figs. 4, 6, and 7;

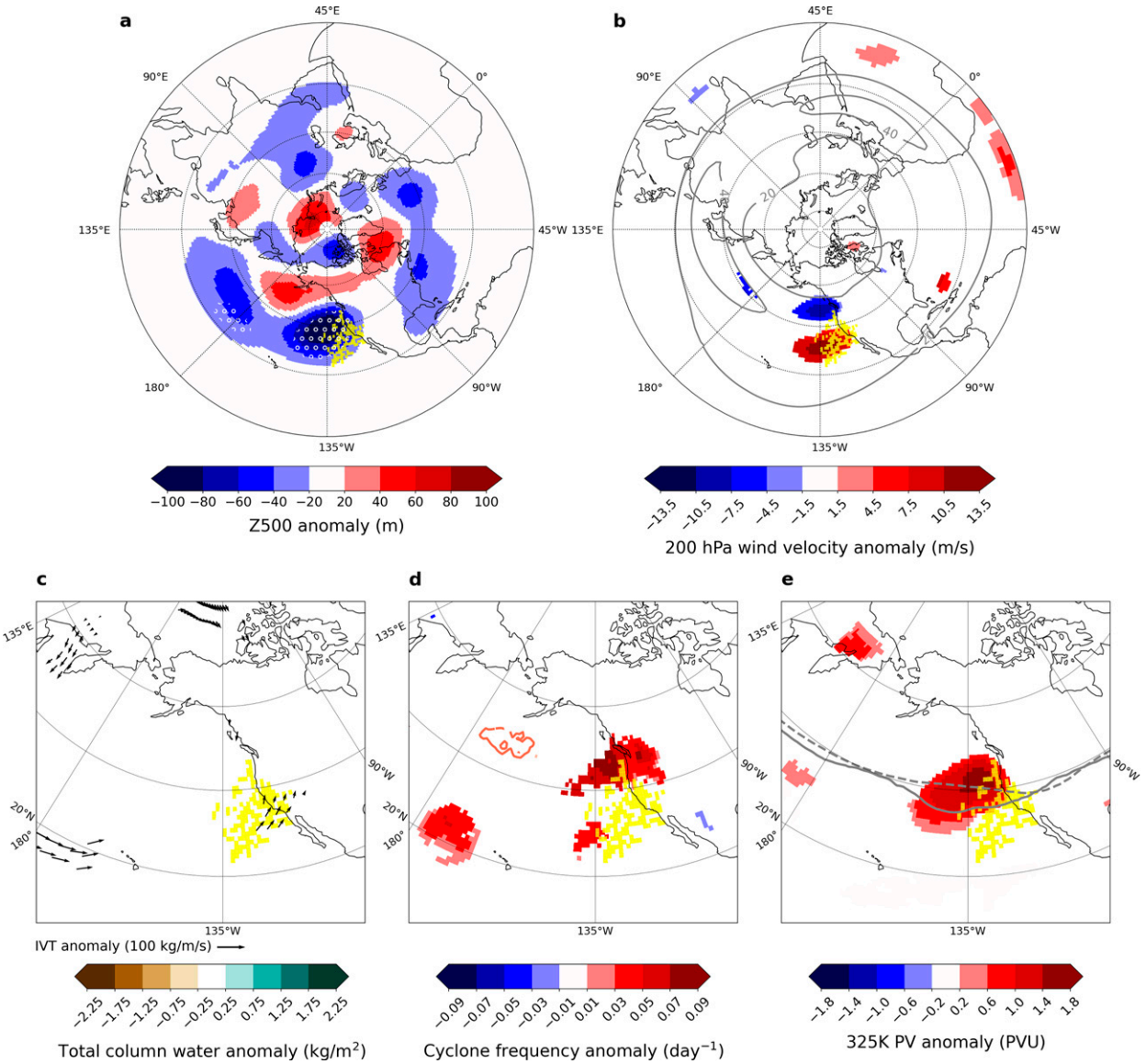

FIG. 7. As in Fig. 5, but for MAM region 2, with PV on the 325-K isentropic surface.

see also Figs. S5 and S6 in the online supplemental material) all exhibit pronounced troughs somewhere along the northwest American coastline during TCEP periods. In DJF, the jet is stronger over the central Pacific and weaker over eastern North America (Fig. 6b) where we detect highly amplified flow (Fig. 6a). PV anomalies point to cyclonic RWB around 120°W, resulting in low-PV intrusions over Canada and weak anomalous poleward IVT along the North American west coast (Fig. 6c). The southern half of the region likely experiences quasigeostrophic lifting ahead of the trough, while moisture availability is not constraining (no TCW/IVT anomalies there). Over northern Canada, cyclones are more frequent (Fig. 6d), and warm conveyor belts possibly provide the lifting and moisture transport responsible for extreme precipitation (Fig. 6c).

By contrast, region 2 in MAM is confined to the northwest American coastline (Fig. 7). TCEP there occurs in conjunction with a trough over the northeastern Pacific. The North Pacific jet is stronger and displaced southward in its exit region around 135°W (Fig. 7b). Enhanced cyclonic activity in the left exit region (Fig. 7d) likely leads to quasigeostrophic lifting and southerly moisture advection (Fig. 7c). Orographic lifting over California probably also plays a role. Positive PV anomalies steepen the meridional PV gradient around 40°N (Fig. 7e), which may lead to a waveguide (Martius et al. 2010) and help explain the persistence in the circulation anomalies. We also detect significant positive SST anomalies over the eastern subtropical Pacific (Fig. S7a in the online supplemental material). Unlike in DJF, we find no clear evidence of RWB; instead, TCEP seems to result from a recurrent hemispheric wave train

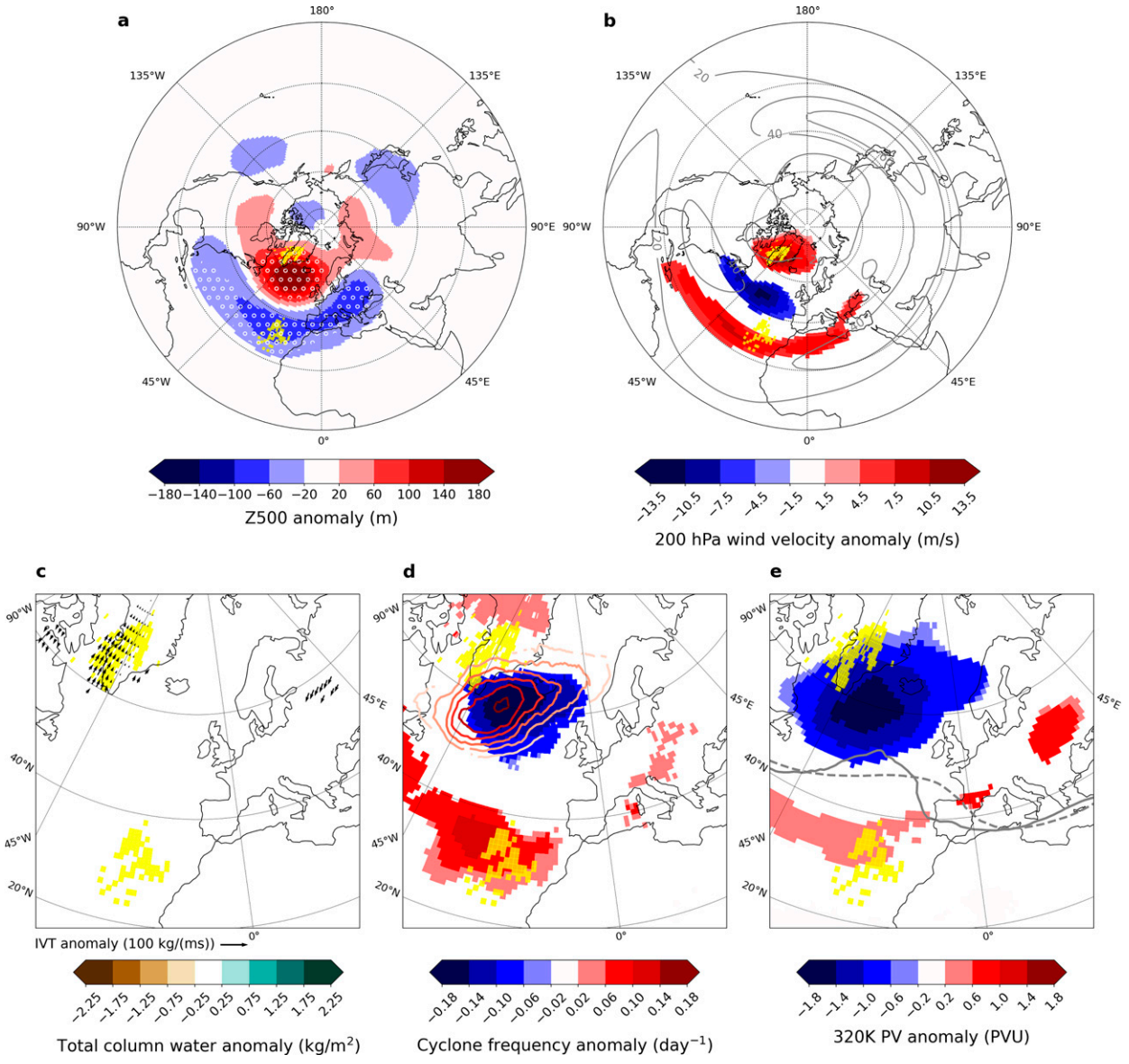

FIG. 8. As in Fig. 5, but for DJF region 5.

at 40°N with wavenumber ≈ 5 (Fig. 7a), which translates into a persistent trough over western North America.

2) NORTH ATLANTIC

As in the North Pacific, the regionalization yields many spatially coherent regions along the eastern and northern margins of the North Atlantic Ocean. Several of these also consist of two parts, one at high latitudes around Greenland and the other in the subtropics or midlatitudes of the eastern North Atlantic (region 5 in DJF, regions 1 and 5 in MAM, and region 1 in SON; Fig. 4). Overall, circulation anomalies for these regions are similar to those in the North Pacific. DJF regions 5 and 7 are both associated with blocking to the south of Greenland and to large-scale anomalies similar to that of the negative NAO phase: a ridge in the North Atlantic and a trough stretching from eastern North America to western Russia (Figs. 8a and 9a). Region 5 exhibits a double-jet situation, in which the eddy-driven jet is shifted northward and the subtropical jet extends farther northward (Fig. 8b). The shape of the dynamical tropopause suggests anticyclonic RWB south of the block (Fig. 8e) where quasigeostrophic lifting likely explains the more frequent cyclones (Fig. 8d). Moisture availability is however not constraining (Fig. 8c). We also detect enhanced cyclone frequency upstream of the block, with warm conveyor belts likely responsible for anomalous poleward IVT (Figs. 8c,d). Results are closely similar for MAM region 1 (Fig. S8 in the online supplemental material).

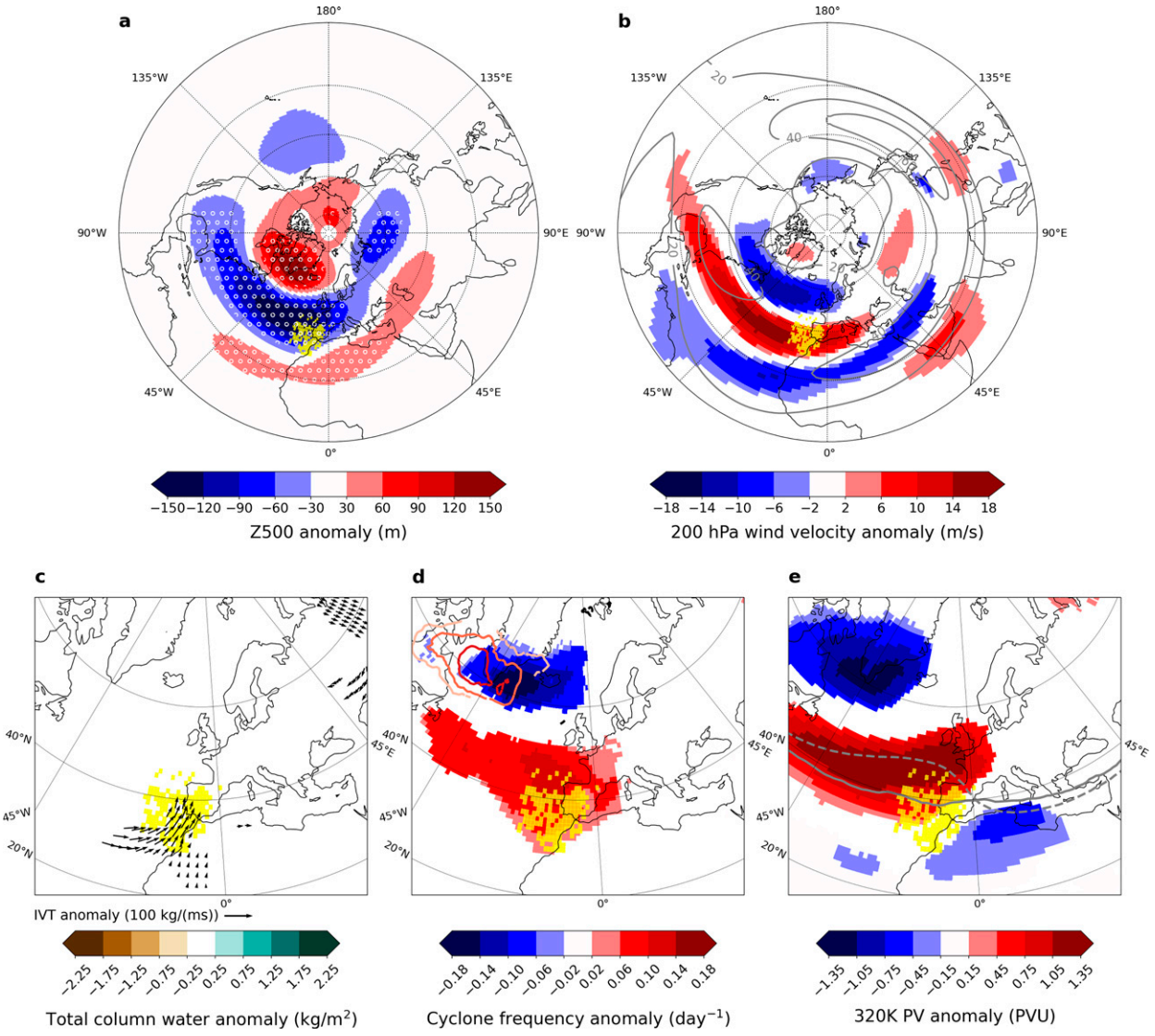

FIG. 9. As in Fig. 5, but for DJF region 7.

By contrast, region 7 over the Iberian Peninsula and northern Morocco shows a southward displacement of the midlatitude jet with no evidence for RWB (Fig. 9b). In the left exit area, northwest of the Iberian Peninsula, we find more frequent cyclones (Fig. 9d) whose warm conveyor belts provide lifting and enhanced southerly IVT (Fig. 9c).

Region 6 in JJA (Figs. 4c and 10) extends over the eastern Atlantic between 40°N and 55°N. There, we detect a hemispheric wave-like Z500 pattern with wavenumber ≈ 5, characterized by a marked trough west of Europe (Fig. 10a), leading to enhanced IVT toward the continent (Fig. 10c). The jet is shifted southward in its exit region (Fig. 10b), and cyclones are more frequent in the left exit region (Fig. 10d).

3) CONTINENTAL EUROPE

We conclude our analysis with region 3 in DJF and region 4 in SON over the European continent (Fig. 4). DJF region 3 is associated with a strong North Atlantic jet, zonally extended over western Europe where it is wedged between a trough to the north and ridge to the south (Figs. 11a,b). These anomalies are consistent with the zonally straight dynamical tropopause and enhanced meridional PV gradient over Europe, which may generate a waveguide (Fig. 11e). Cyclones are more frequent in the left exit region over the North Sea and less frequent in the right exit region over the Mediterranean (Fig. 11d). The trailing cold fronts of the North Sea cyclones could cause the extreme precipitation in the European midlatitudes, while warm conveyor belts may explain the occurrence of extreme precipitation in Scandinavia. The absence of significant IVT or TCW anomalies suggests that moisture availability is not key to explaining TCEP. However, we do find significant SST anomalies in the eastern North Pacific, somewhat similar to the negative Pacific decadal oscillation pattern (Fig. S7c in the online supplemental material).

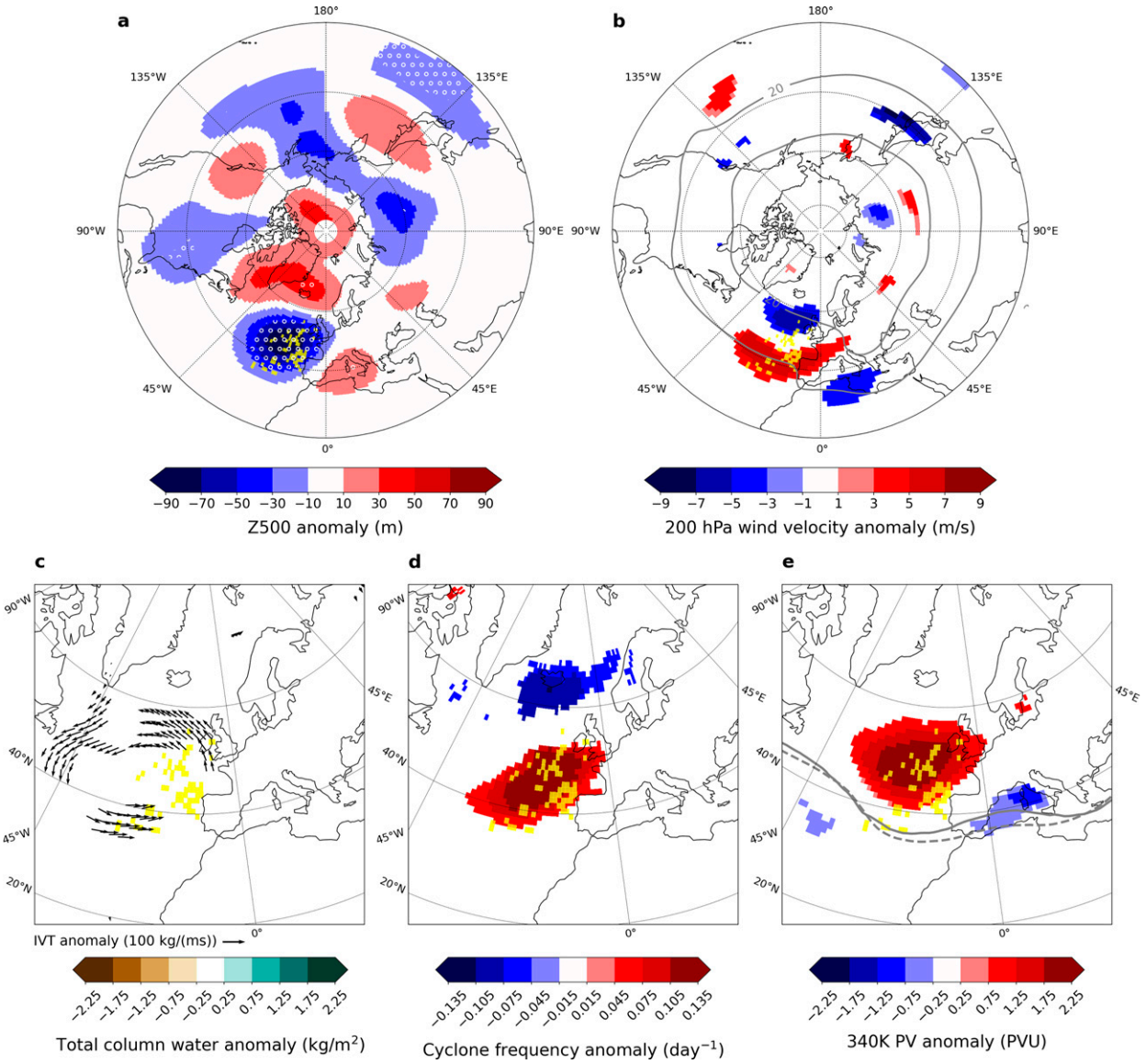

FIG. 10. As in Fig. 5, but for JJA region 6, with PV on the 340-K isentropic surface.

For SON region 4, western Europe is also under a trough, but the flow is not zonal (Fig. 12e). On the contrary, we find an amplified flow over Europe and Z500 anomalies exhibit a hemispheric wave pattern with wavenumber ≈ 4 (Figs. 12a,d). Enhanced ocean-to-continent IVT leads to deep moisture penetration into northern Europe (Fig. 12c). Ahead of the trough, quasigeostrophic lifting of moist North Atlantic air likely accounts for extreme precipitation, while farther downstream quasigeostrophic lifting of moist Mediterranean air combines with orographic lifting (Fig. 12c).

4. Discussion

a. Spatiotemporal distribution of TCEP

The skill of the Poisson GLM in reproducing temporal variability in extreme event count varies substantially across space and time (Fig. 2). High model skill indicates the strong influence of atmospheric dynamics on TCEP likelihood. However, the opposite is not necessarily true. In particular, if TCEP is too rare (for instance 1–2 events only during the 1979–2019 period), it may become difficult for the model to correctly capture a link to large-scale circulation. ERA5 provides roughly 175 values in each season to train the model. Still, even in DJF, when TCEP is most frequent, the average grid point experiences more than two precipitation extremes within 3 weeks only 3 times out of 175. Only 15% of grid points have five or more TCEP periods. Consequently, at the hemispheric scale, model skill tends to increase with TCEP frequency (Fig. S9 in the online supplemental material). Nevertheless, one should not conclude that high model skill can only be achieved with high TCEP frequencies. In DJF, for instance, of all the grid points with fewer than two TCEP periods, 14% exhibit DR values larger than 0.25, and 60% of

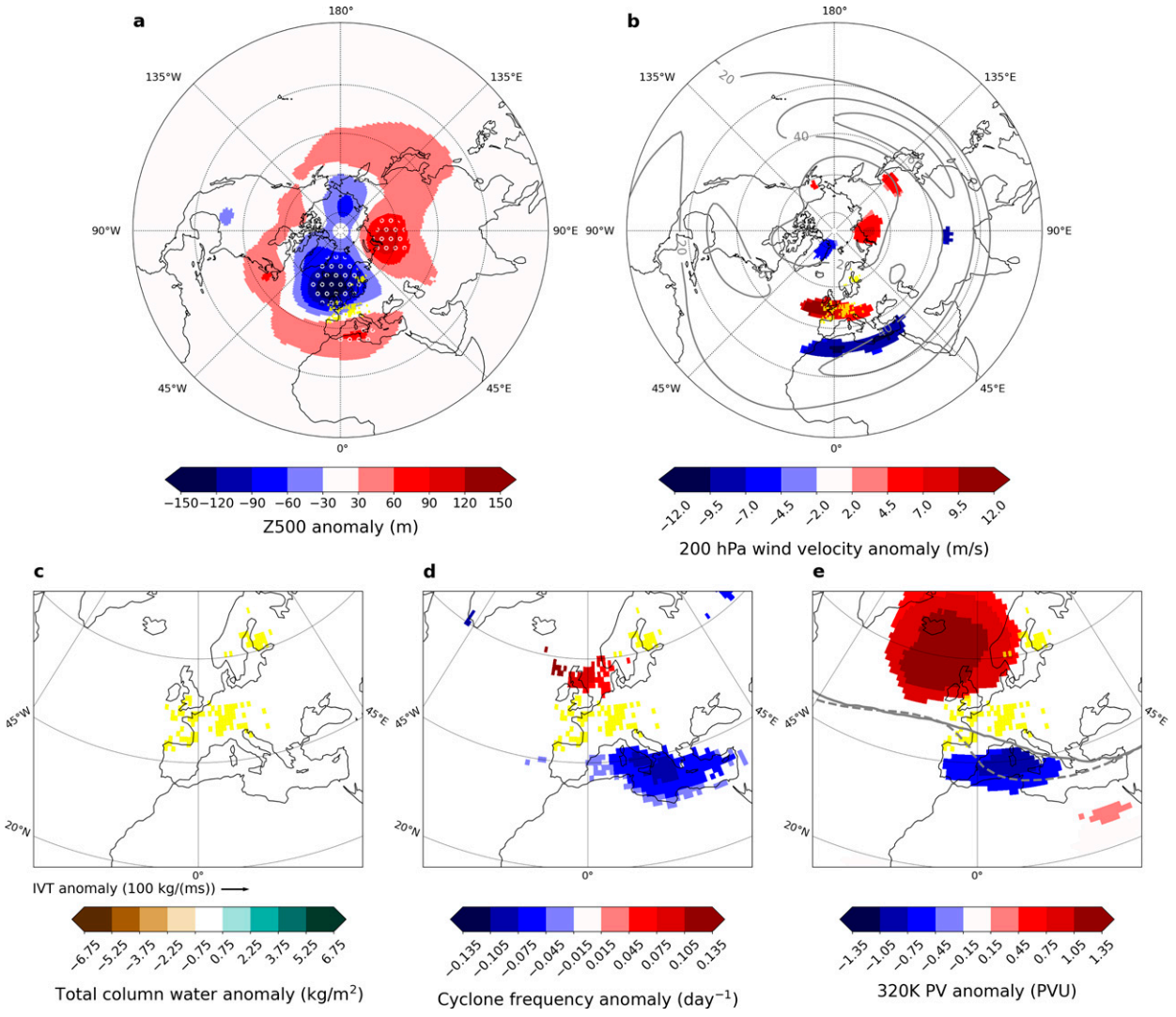

FIG. 11. As in Fig. 5, but for DJF region 3.

grid points where DR ≥0.25 experience three or fewer TCEP periods.

A comparison can be made with the results of Tuel and Martius (2021), who analyzed the statistical significance of TCEP in ERA5 using the same seasonal framework as in the present study. Areas with high statistical significance generally experience more TCEP events than regions where no statistical significance is found. Although the seasonal cycle and spatial distribution of statistical significance found by Tuel and Martius (2021) shows some overlap with the results in Fig. 2, high DR values are not restricted to areas exhibiting statistically significant clustering. This is particularly true at high latitudes for much of the year, over western Europe/the eastern Atlantic in JJA and SON, and along the western North American coastline outside the winter season. By contrast, some areas with statistically significant TCEP do not stand out on the GLM-based DR maps. This is the case for the equatorial Pacific Ocean, where DR values are large in DJF only, whereas statistical significance is found in all seasons (Tuel and Martius 2021). This discrepancy may arise because our covariates may not be most relevant in the tropics, where Z500 anomalies are generally weak. Using the streamfunction instead in similar analysis confined to the tropics (20°S–20°N) could be better.

b. *Physical drivers of TCEP*

TCEP occurs when three ingredients are combined: lifting, moisture availability, and persistence of atmospheric conditions. Results showed that a wide range of processes can provide these ingredients. Nonetheless, a number of similarities emerge (Fig. 13). We now summarize and analyze regional circulation anomalies by focusing on processes common to several regions.

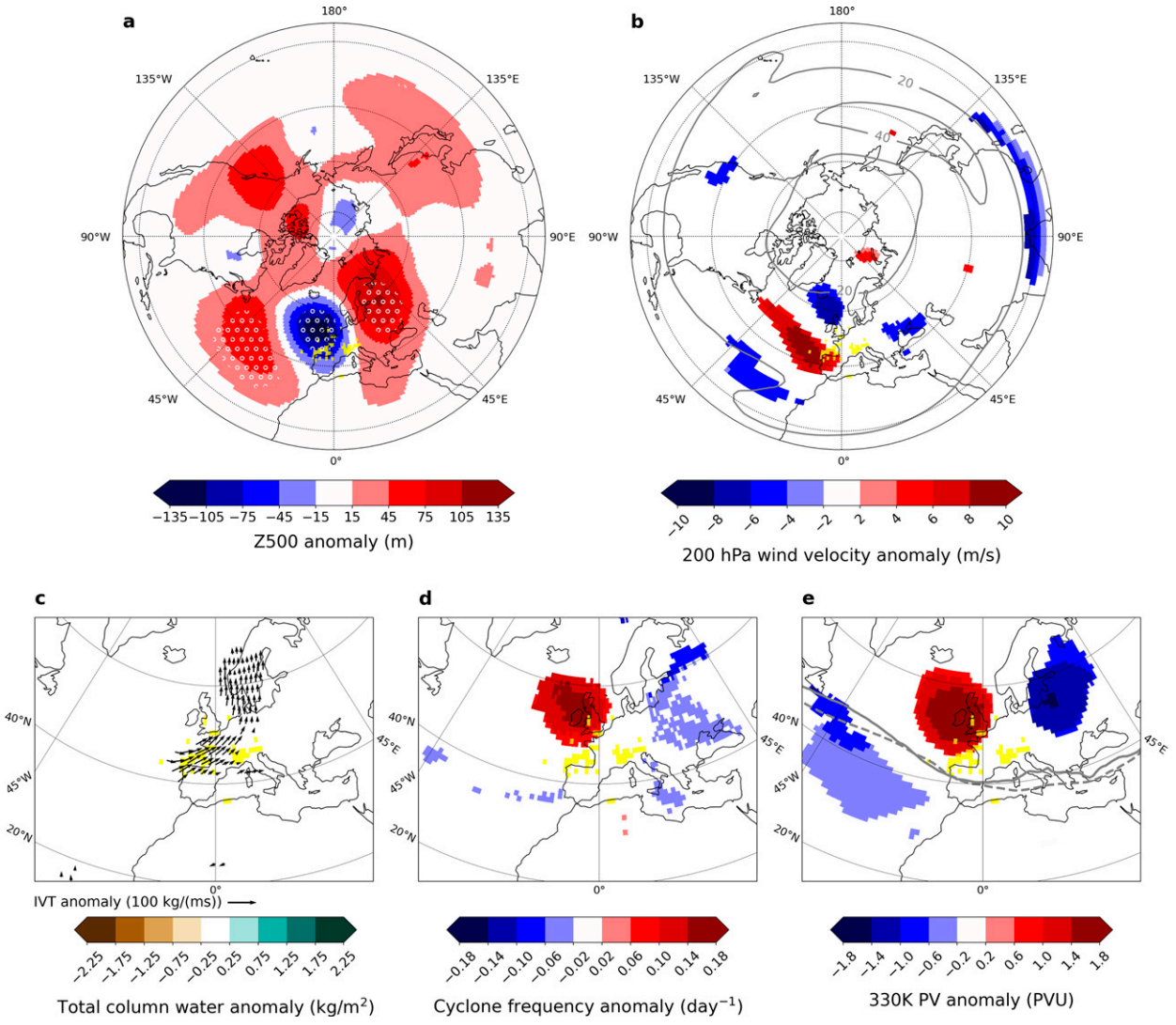

FIG. 12. As in Fig. 5, but for SON region 4, with PV on the 330-K isentropic surface.

1) BLOCKING

Blocking is an important factor responsible for the GLM model's high skill over the high latitudes and eastern margins of ocean basins (Fig. 2). Indeed, blocking over the Gulf of Alaska and south of Greenland strongly influences the likelihood of extreme precipitation both upstream and downstream of blocked areas: the Bering Strait and North America's western coast in the Pacific, and Greenland and southwestern Europe and the eastern subtropical Atlantic in the Atlantic (Figs. 5 and 9; see also Figs. S3, S4, S6, and S8 in the online supplemental material). Numerous previous studies have discussed this relationship (e.g., Yao and De-Hai 2014; Sousa et al. 2017; Lenggenhager and Martius 2019; Pasquier et al. 2019).

Blocking can divert cyclones poleward upstream of the blocked area and cause meridionally amplified flow and anticyclonic RWB downstream (Altenhoff et al. 2008). RWB then leads to high-PV intrusions at low latitudes, often as PV streamers and cutoffs that may be associated with atmospheric rivers (Payne and Magnusdottir 2014; Lenggenhager and Martius 2019; Pasquier et al. 2019; de Vries 2021). Lifting and moisture in the upstream cyclonic warm conveyor belts account for extreme precipitation at high latitudes. Downstream of the block, lifting is rather forced by upper-level divergence ahead of the PV intrusions which, coupled with high subtropical atmospheric moisture, leads to extreme precipitation (de Vries 2021).

The persistence (and high GLM DR values) may arise because blocking is most frequent above the North Atlantic and Pacific Oceans, especially during winter (Tibaldi et al. 1994; Rohrer et al. 2020). Blocking persistence in these two locations therefore emerges as an important driver of TCEP in Europe and North America. Because we consider 3-week mean anomalies, we cannot conclude whether such persistence results from particularly long-lived blocks or recurrent short-lived blocks, and whether

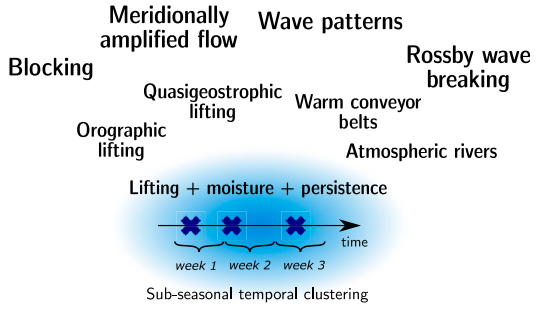

FIG. 13. Key processes leading to subseasonal temporal clustering: atmospheric configurations such as blocking favor recurrent or persistent lifting and moisture transport, which in turn result in the temporal clustering of precipitation extremes over subseasonal time scales.

TCEP is associated with repeated or persistent wavebreaking downstream of the blocks.

2) QUASI-STATIONARY AND RECURRENT PLANETARY WAVES

Hemispheric wave-like patterns in the Z500 anomalies, associated with jet streaks, persistent troughs, and enhanced IVT and moisture convergence, are common to several regions along the western European and North American coastlines (Figs. 7, 10, and 12). Quasigeostrophic lifting forced by upper-level divergence occurs ahead of the trough, in conjunction with anomalous IVT structures that possibly indicate atmospheric rivers. A steeper meridional PV gradient and stronger jet may act as waveguides and explain the persistence of extreme precipitation.

Such conditions may have various origins. One possibility is stationary or quasi-stationary planetary waves, which several studies have shown were related to persistent temperature and precipitation extremes around the world, especially during summer (e.g., Petoukhov et al. 2013; Coumou et al. 2014; Kornhuber et al. 2017). The amplitude of quasi-stationary waves tends to peak in the storm track exit regions over Europe and western North America (Wolf et al. 2018), precisely where TCEP is associated with hemispheric wave-like patterns. In addition to quasi-stationary flow, recurrent Rossby wave packets (RRWPs) may also result in hemispheric wave-like patterns at the 3-week time scale. RRWPs are characterized by the repeated formation of synoptic-scale transient troughs and ridges at the same longitudes. They are known to modulate the persistence of hot/cold (Röthlisberger et al. 2019) and wet/dry (Ali et al. 2021) spells in the midlatitudes. TCEP is systematically linked to high-PV anomalies above the regions, but only in the case of SON region 4 (Fig. 12) do we detect significant negative PV anomalies upstream and downstream of the region.

Our results cannot clarify whether Z500 patterns arise from quasi-stationarity and/or recurrence of transient flow patterns. In SON region 4, RRWPs were responsible for the repeated occurrence of extreme precipitation at least once, in the autumn of 1993 (Barton et al. 2016). Focusing on four TCEP episodes in the southern Alps in Switzerland, Barton et al. (2016) nevertheless concluded that dynamical drivers varied depending on the episode and were usually found in combination. Some features were common to all episodes, including strong phase locking of the midlatitude flow leading to extreme poleward IVT converging on the southern side of the Alps, which are also robust in our results (Fig. 12). Interestingly, TCEP is detected for JJA region 6 (Fig. 4) in June 2007, a period when England, at the eastern edge of the region, also experienced several extreme precipitation events (13–15 and 25 June). Blackburn et al. (2008) found that the 2007 event was related to a persistent trough over England that was part of an almost stationary hemispheric wave pattern with wavenumber ≈6. The jet stream was stronger than average over Europe and displaced equatorward not only over France and Spain but also over the Pacific, the Middle East, and North America. We find similar circulation anomalies linked to the recurrent formation of extreme precipitation events in this region (Figs. 10a,b), although the Z500 wave pattern projects more strongly onto wavenumber 5 in our case.

3) MERIDIONALLY AMPLIFIED FLOW

TCEP may also be associated with locally amplified flow, leading to persistent troughs but not necessarily forced by upstream blocking. Such appears to be the case for DJF region 4 in North America (Fig. 6) and region 11 in Southwest Asia (Fig. S10 in the online supplemental material), albeit for different reasons. Over North America, the amplified flow pattern is associated with cyclonic RWB-type anomalies along the continent's western coastline (Fig. 6e) with no latitudinal shift in the position of the jet but a slightly more intense jet core than average upstream over the northwestern Pacific (Fig. 6b). By contrast, the amplified flow in region 11 is connected to a clear equatorward shift of the North African jet (Fig. S10b). In both cases, quasigeostrophic lifting occurs ahead of the trough, with no significant increase in cyclonic activity. In the northwestern Pacific, moisture availability is not constraining, unlike in Southwest Asia, where moisture exports from the tropics are critical.

c. *TCEP over Europe during winter and connection to large-scale climate indices*

We finish by discussing the two DJF European regions (regions 3 and 7; Fig. 4a). Region 3 consists of two parts, one that extends roughly over England, France, Germany, and Switzerland, and one over Finland and Sweden. Yang and Villarini (2019) argued for a link between the likelihood of TCEP and the NAO index in this region, but we find that the NAO is not the best explanatory variable for TCEP there. The jet is not displaced poleward but becomes more intense and elongated in its exit region; this can also be seen in the dynamical tropopause composite, which shows a much straighter jet over Europe (Fig. 11) (Woollings et al. 2010; Mahlstein et al. 2012; Madonna et al. 2017). Such conditions were already detected in connection with serial cyclone clustering over the United Kingdom in winter (Pinto et al. 2014). The associated Z500 anomalies to some extent resemble the superposition of a positive Arctic Oscillation phase and a negative east Atlantic

phase, but without fully projecting onto any the leading modes of winter interannual circulation variability in the Euro-Atlantic sector. Instead, they are reminiscent of the "Atlantic trough" regime identified in Grams et al. (2017). Pasquier et al. (2019) found that this regime was linked to more frequent atmospheric rivers and precipitation extremes from northwestern Spain to southern Scandinavia, in accordance with the spatial structure of region 3. Our results suggest that this enhancement of atmospheric river activity is related to the clustering of midlatitude cyclones over Scotland and Denmark, cyclones that can increase moisture penetration along their warm fronts. The straight jet may be maintained by RWB on its northern and southern flanks, as was the case during the 2013/14 winter, which saw major cyclone clustering over the British Isles (Priestley et al. 2017).

By contrast, circulation anomalies for region 7, which covers Morocco, the Iberian Peninsula, and the ocean directly to the west, strongly project onto the negative NAO phase, displaying a clear southward shift and deeper eastward penetration of the Atlantic storm track (Figs. 9a,b). They are also similar to the "Greenland blocking" regime of Grams et al. (2017), which, like a negative NAO, is associated with more frequent cyclones and increased moisture transport by atmospheric rivers over southwestern Europe (Pasquier et al. 2019). In this region, the NAO index thus appears to be a valid predictor of TCEP, and our results are consistent with those of Yang and Villarini (2019).

d. *Some limitations and future prospects*

Our results are subject to several limitations. First, the statistical and co-occurrence analyses discussed above are not sufficient to demonstrate causality, only the consistency between anomalies of certain variables and TCEP occurrence in selected regions. Several of these anomalies can either lead to or result from the occurrence of precipitation extremes. Diabatic PV depletion downstream of heavy precipitation can lead to or enhance blocking and contribute to the hemispheric-scale phase locking observed in several regions (section 4b). Similarly, certain Z500 anomaly fields, for instance the NAO-like patterns in the European sector (section 4c), can be partly maintained through RWB linked to the cyclones embedded in the overall pattern (Benedict et al. 2004).

Second, averaging Z500 values over 3 weeks can hide short-term variability in atmospheric conditions. The GLM model may thus miss important Z500 variability at short time scales that is smoothed in the 3-week averages. The a posteriori analysis of specific regions allows partial compensation of this difficulty by considering cyclone frequency anomalies. Analyses could be expanded by looking at individual cyclone tracks, atmospheric rivers, and blocking events instead of frequency anomalies. Because we have exclusively looked at average conditions associated with TCEP, this could also help better understand the potential diversity in atmospheric conditions linked to TCEP. Certain factors that are not statistically significant in our results may still play a role in specific events, as in Barton et al. (2016). The choice of the 3-week window for subseasonal clustering can also be questioned. It is suited to analyze TCEP at subseasonal time scales, but so are 2- and 4-week windows. We repeated our spatial clustering analysis with 2-week windows and found closely similar results (Figs. S11 and S12 in the online supplemental material), although some differences can be seen. It would be worthwhile to assess the robustness of the various physical mechanisms we identified to the choice of the time window. While we exclusively focus on subseasonal time scales, it is important to mention that results could differ for shorter or longer time scales. Dacre and Pinto (2020) discussed, in the case of extratropical cyclones, that dynamical features linked to temporal clustering varied as a function of the time window (from a few days to multidecadal). At short time scales, cyclone clustering is more often related to secondary cyclogenesis within cyclone families, whereas at subseasonal to decadal time scales it is strongly determined by large-scale patterns of variability such as the NAO. The strength of that link also varies with the time scale, peaking around 3 months for the NAO (Vitolo et al. 2009). Our results nevertheless provide two important pieces of information. First, they indicate regions of the Northern Hemisphere which should be analyzed as a whole for TCEP. Our approach allows an optimal, data-informed selection of regions that classical regression maps do not detect. Second, our results are an important first step to identifying the most likely physical drivers of TCEP and to building and evaluating informed causal networks. This would allow testing of more refined hypotheses on why and where TCEP occurs, for instance within idealized frameworks.

In addition, unlike certain previous regionalization approaches for extremes (Bernard et al. 2013; Saunders et al. 2021), it is not free from distributional assumptions. As shown by Fig. S1 in the online supplemental material, the Poisson assumption is not valid in some regions, where our approach may fail to detect links between large-scale dynamics and TCEP. This in itself does not compromise our results, which focused on the mid-to-high latitudes, where the Poisson assumption is verified. Additionally, tropical regions where the Poisson goodness of fit fails also exhibit small DR values and are thus excluded from the regionalization.

As mentioned in section 2a, ERA5 precipitation data are subject to limitations. They compare well to satellite- and station-based products from the tropics to the midlatitudes for extreme precipitation timing and magnitude (Rivoire et al. 2021; Tuel and Martius 2021). ERA5's robustness at high latitudes, where few observation-based datasets are available, is more difficult to assess. At such latitudes, the areas of high model skill exhibit at least strong physical consistency, but it could be that some of the numerous high-latitude regions in Fig. 4 are less physically relevant than others. Note that since we define extremes based on daily percentiles in ERA5, our results are unaffected by biases in these percentiles. Averaging extreme event counts over 3 weeks also smooths the effects of unavoidable errors in the timing of extremes.

5. Conclusions

In this study, we used Poisson regression to assess the influence of large-scale Z500 variability in TCEP likelihood across the Northern Hemisphere. By implementing a *k*-means algorithm on the regression coefficients, we then created regionalizations for each season. We obtained spatially coherent regions, some noted in the literature, but several others not

mentioned before. We then discussed the processes associated with TCEP for several regions with respect to the three key ingredients required for TCEP to occur: lifting, moisture availability, and persistence. Many regions are located at high latitudes and over the eastern halves of the ocean basins, but some are also found in the tropics and subtropics in DJF and MAM.

TCEP is generally related to distinct cyclone and blocking frequency anomalies and upper-level circulation patterns that provide upward motion. IVT and precipitable water anomalies are not always detected, especially close to the subtropics, which means that forced lifting alone is often sufficient to trigger heavy precipitation. Blocking is especially important in winter and spring over the mid- to high latitudes of the North Atlantic and Pacific Oceans, where it triggers TCEP by deflecting cyclones upstream of blocked areas and causing wave breaking downstream. Zonally extended wave patterns and persistent troughs are found in association with TCEP over western Europe in summer and autumn and the Canadian Arctic and California in winter. Persistent SST anomalies in the tropics seem to favor TCEP occurrence in tropical areas but generally have little influence in the extratropics.

Our regionalization contributes to improving the understanding and mitigation of the risks related to TCEP. For instance, it could be used to model precipitation extremes at regional scales with robust dependence structures and climatic covariates (Davison et al. 2012). Our results may also help assess the performance of weather and climate models in reproducing TCEP statistics in present and future climates. One potential avenue of research could compare the skill of numerical models in forecasting TCEP at subseasonal time scales with that of statistical models based on the knowledge of Z500 anomaly fields associated with TCEP.

Acknowledgments. We thank three anonymous reviewers for their thoughtful comments that helped to improve the quality of the paper. Author Martius acknowledges support from the Swiss Science Foundation (SNSF) Grant 178751. The authors gratefully acknowledge the help of S. Mubashshir Ali, who calculated the PV data; Simon Milligan, for his feedback on the draft; and Marco Rohrer, for providing the blocking and cyclone frequency indices.

Data availability statement. ERA5 reanalysis data are available for 1979–2019 online (https://doi.org/10.24381/cds.adbb2d47).

REFERENCES

Ali, S. M., O. Martius, and M. Röthlisberger, 2021: Recurrent Rossby wave packets modulate the persistence of dry and wet spells across the globe. *Geophys. Res. Lett.*, **48**, e2020GL091452, https://doi.org/10.1029/2020GL091452.

Altenhoff, A. M., O. Martius, M. Croci-Maspoli, C. Schwierz, and H. C. Davies, 2008: Linkage of atmospheric blocks and synoptic-scale Rossby waves: A climatological analysis. *Tellus*, **60A**, 1053–1063, https://doi.org/10.1111/j.1600-0870.2008.00354.x.

Barton, Y., P. Giannakaki, H. von Waldow, C. Chevalier, S. Pfahl, and O. Martius, 2016: Clustering of regional-scale extreme precipitation events in southern Switzerland. *Mon. Wea. Rev.*, **144**, 347–369, https://doi.org/10.1175/MWR-D-15-0205.1.

Benedict, J. J., S. Lee, and S. B. Feldstein, 2004: Synoptic view of the North Atlantic Oscillation. *J. Atmos. Sci.*, **61**, 121–144, https://doi.org/10.1175/1520-0469(2004)061<0121:SVOTNA>2.0.CO;2.

Bernard, E., P. Naveau, M. Vrac, and O. Mestre, 2013: Clustering of maxima: Spatial dependencies among heavy rainfall in France. *J. Climate*, **26**, 7929–7937, https://doi.org/10.1175/JCLI-D-12-00836.1.

Blackburn, M., J. Methven, and N. Roberts, 2008: Large-scale context for the UK floods in summer 2007. *Weather*, **63**, 280–288, https://doi.org/10.1002/wea.322.

Catto, J. L., and S. Pfahl, 2013: The importance of fronts for extreme precipitation. *J. Geophys. Res. Atmos.*, **118**, 10 791–10 801, https://doi.org/10.1002/jgrd.50852.

Coles, S., 2001: *An Introduction to Statistical Modeling of Extreme Values*. Springer, 209 pp., https://doi.org/10.1007/978-1-4471-3675-0.

Coumou, D., V. Petoukhov, S. Rahmstorf, S. Petri, and H. J. Schellnhuber, 2014: Quasi-resonant circulation regimes and hemispheric synchronization of extreme weather in boreal summer. *Proc. Natl. Acad. Sci. USA*, **111**, 12 331–12 336, https://doi.org/10.1073/pnas.1412797111.

Dacre, H. F., and J. G. Pinto, 2020: Serial clustering of extratropical cyclones: A review of where, when and why it occurs. *npj Climate Atmos. Sci.*, **3**, 48, https://doi.org/10.1038/s41612-020-00152-9.

Davies, H. C., 2015: Weather chains during the 2013/2014 winter and their significance for seasonal prediction. *Nat. Geosci.*, **8**, 833–837, https://doi.org/10.1038/ngeo2561.

Davison, A. C., S. A. Padoan, and M. Ribatet, 2012: Statistical modeling of spatial extremes. *Stat. Sci.*, **27**, 161–186, https://doi.org/10.1214/11-STS376.

de Vries, A. J., 2021: A global climatological perspective on the importance of Rossby wave breaking and intense moisture transport for extreme precipitation events. *Wea. Climate Dyn.*, **2**, 129–161, https://doi.org/10.5194/wcd-2-129-2021.

Doswell, C. A., H. E. Brooks, and R. A. Maddox, 1996: Flash flood forecasting: An ingredients-based methodology. *Wea. Forecasting*, **11**, 560–581, https://doi.org/10.1175/1520-0434(1996)011<0560:FFFAIB>2.0.CO;2.

Ester, M., H.-P. Kriegel, J. Sander, and X. Xu, 1996: *A Density-Based Algorithm for Discovering Clusters in Large Spatial Databases with Noise*. AAAI Press, 226–231.

Fränti, P., and S. Sieranoja, 2019: How much can *k*-means be improved by using better initialization and repeats? *Pattern Recognit.*, **93**, 95–112, https://doi.org/10.1016/j.patcog.2019.04.014.

Friedman, J., T. Hastie, and R. Tibshirani, 2010: Regularization paths for generalized linear models via coordinate descent. *J. Stat. Softw.*, **33** (1), 1–22, https://doi.org/10.18637/jss.v033.i01.

Gimeno, L., A. Drumond, R. Nieto, R. M. Trigo, and A. Stohl, 2010: On the origin of continental precipitation. *Geophys. Res. Lett.*, **37**, L13804, https://doi.org/10.1029/2010GL043712.

Grams, C. M., R. Beerli, S. Pfenninger, I. Staffell, and H. Wernli, 2017: Balancing Europe's wind-power output through spatial deployment informed by weather regimes. *Nat. Climate Change*, **7**, 557–562, https://doi.org/10.1038/nclimate3338.

Hersbach, H., and Coauthors, 2020: The ERA5 global reanalysis. *Quart. J. Roy. Meteor. Soc.*, **146**, 1999–2049, https://doi.org/10.1002/qj.3803.

Huntingford, C., and Coauthors, 2014: Potential influences on the United Kingdom's floods of winter 2013/14. *Nat. Climate Change*, **4**, 769–777, https://doi.org/10.1038/nclimate2314.

Kopp, J., P. Rivoire, S. M. Ali, Y. Barton, and O. Martius, 2021: A novel method to identify sub-seasonal clustering episodes of extreme precipitation events and their contributions to large accumulation periods. *Hydrol. Earth Syst. Sci.*, **25**, 5153–5174, https://doi.org/10.5194/hess-25-5153-2021.

Kornhuber, K., V. Petoukhov, D. Karoly, S. Petri, S. Rahmstorf, and D. Coumou, 2017: Summertime planetary wave resonance in the Northern and Southern Hemispheres. *J. Climate*, **30**, 6133–6150, https://doi.org/10.1175/JCLI-D-16-0703.1.

Lamb, D., 2001: Rain production in convective storms. *Severe Convective Storms, Meteor. Monogr.*, No. 50, Amer. Meteor. Soc., 299–321, https://doi.org/10.1007/978-1-935704-06-5_8.

Lenggenhager, S., and O. Martius, 2019: Atmospheric blocks modulate the odds of heavy precipitation events in Europe. *Climate Dyn.*, **53**, 4155–4171, https://link.springer.com/article/10.1007/s00382-019-04779-0.

Madonna, E., C. Li, C. M. Grams, and T. Woollings, 2017: The link between eddy-driven jet variability and weather regimes in the North Atlantic–European sector. *Quart. J. Roy. Meteor. Soc.*, **143**, 2960–2972, https://doi.org/10.1002/qj.3155.

Mahlstein, I., O. Martius, C. Chevalier, and D. Ginsbourger, 2012: Changes in the odds of extreme events in the Atlantic basin depending on the position of the extratropical jet. *Geophys. Res. Lett.*, **39**, L22805, https://doi.org/10.1029/2012GL053993.

Mailier, P. J., D. B. Stephenson, C. A. T. Ferro, and K. I. Hodges, 2006: Serial clustering of extratropical cyclones. *Mon. Wea. Rev.*, **134**, 2224–2240, https://doi.org/10.1175/MWR3160.1.

Martius, O., C. Schwierz, and H. C. Davies, 2010: Tropopause-level waveguides. *J. Atmos. Sci.*, **67**, 866–879, https://doi.org/10.1175/2009JAS2995.1.

——, and Coauthors, 2013: The role of upper-level dynamics and surface processes for the Pakistan flood of July 2010. *Quart. J. Roy. Meteor. Soc.*, **139**, 1780–1797, https://doi.org/10.1002/qj.2082.

Moore, B. J., A. B. White, D. J. Gottas, and P. J. Neiman, 2020: Extreme precipitation events in Northern California during winter 2016–17: Multiscale analysis and climatological perspective. *Mon. Wea. Rev.*, **148**, 1049–1074, https://doi.org/10.1175/MWR-D-19-0242.1.

Nieto, R., D. Ciric, M. Vázquez, M. L. Liberato, and L. Gimeno, 2019: Contribution of the main moisture sources to precipitation during extreme peak precipitation months. *Adv. Water Resour.*, **131**, 103385, https://doi.org/10.1016/j.advwatres.2019.103385.

Pasquier, J. T., S. Pfahl, and C. M. Grams, 2019: Modulation of atmospheric river occurrence and associated precipitation extremes in the North Atlantic region by European weather regimes. *Geophys. Res. Lett.*, **46**, 1014–1023, https://doi.org/10.1029/2018GL081194.

Payne, A. E., and G. Magnusdottir, 2014: Dynamics of landfalling atmospheric rivers over the North Pacific in 30 years of MERRA reanalysis. *J. Climate*, **27**, 7133–7150, https://doi.org/10.1175/JCLI-D-14-00034.1.

Petoukhov, V., S. Rahmstorf, S. Petri, and H. J. Schellnhuber, 2013: Quasiresonant amplification of planetary waves and recent Northern Hemisphere weather extremes. *Proc. Natl. Acad. Sci. USA*, **110**, 5336–5341, https://doi.org/10.1073/pnas.1222000110.

Pfahl, S., E. Madonna, M. Boettcher, H. Joos, and H. Wernli, 2014: Warm conveyor belts in the ERA-Interim dataset (1979–2010). Part II: Moisture origin and relevance for precipitation. *J. Climate*, **27**, 27–40, https://doi.org/10.1175/JCLI-D-13-00223.1.

Piaget, N., P. Froidevaux, P. Giannakaki, F. Gierth, O. Martius, M. Riemer, G. Wolf, and C. M. Grams, 2015: Dynamics of a local alpine flooding event in October 2011: Moisture source and large-scale circulation. *Quart. J. Roy. Meteor. Soc.*, **141**, 1922–1937, https://doi.org/10.1002/qj.2496.

Pinto, J. G., N. Bellenbaum, M. K. Karremann, and P. M. Della-Marta, 2013: Serial clustering of extratropical cyclones over the North Atlantic and Europe under recent and future climate conditions. *J. Geophys. Res. Atmos.*, **118**, 12 476–12 485, https://doi.org/10.1002/2013JD020564.

——, I. Gómara, G. Masato, H. F. Dacre, T. Woollings, and R. Caballero, 2014: Large-scale dynamics associated with clustering of extratropical cyclones affecting western Europe. *J. Geophys. Res. Atmos.*, **119**, 13 704–13 719, https://doi.org/10.1002/2014JD022305.

Priestley, M. D. K., J. G. Pinto, H. F. Dacre, and L. C. Shaffrey, 2017: The role of cyclone clustering during the stormy winter of 2013/2014. *Weather*, **72**, 187–192, https://doi.org/10.1002/wea.3025.

Rivoire, P., O. Martius, and P. Naveau, 2021: A comparison of moderate and extreme ERA-5 daily precipitation with two observational data sets. *Earth Space Sci.*, **8**, e2020EA001633, https://doi.org/10.1029/2020EA001633.

Rohrer, M., O. Martius, C. C. Raible, and S. Brönnimann, 2020: Sensitivity of blocks and cyclones in ERA5 to spatial resolution and definition. *Geophys. Res. Lett.*, **47**, e2019GL085582, https://doi.org/10.1029/2019GL085582.

Röthlisberger, M., O. Martius, and H. Wernli, 2018: Northern Hemisphere Rossby wave initiation events on the extratropical jet—A climatological analysis. *J. Climate*, **31**, 743–760, https://doi.org/10.1175/JCLI-D-17-0346.1.

——, L. Frossard, L. F. Bosart, D. Keyser, and O. Martius, 2019: Recurrent synoptic-scale Rossby wave patterns and their effect on the persistence of cold and hot spells. *J. Climate*, **32**, 3207–3226, https://doi.org/10.1175/JCLI-D-18-0664.1.

Saunders, K. R., A. G. Stephenson, and D. J. Karoly, 2021: A regionalisation approach for rainfall based on extremal dependence. *Extremes*, **24**, 215–240, https://doi.org/10.1007/s10687-020-00395-y.

Schwierz, C., M. Croci-Maspoli, and H. C. Davies, 2004: Perspicacious indicators of atmospheric blocking. *Geophys. Res. Lett.*, **31**, L06125, https://doi.org/10.1029/2003GL019341.

Smith, R. B., and I. Barstad, 2004: A linear theory of orographic precipitation. *J. Atmos. Sci.*, **61**, 1377–1391, https://doi.org/10.1175/1520-0469(2004)061<1377:ALTOOP>2.0.CO;2.

Sousa, P. M., R. M. Trigo, D. Barriopedro, P. M. M. Soares, A. M. Ramos, and M. L. R. Liberato, 2017: Responses of European precipitation distributions and regimes to different blocking locations. *Climate Dyn.*, **48**, 1141–1160, https://doi.org/10.1007/s00382-016-3132-5.

Tibaldi, S., E. Tosi, A. Navarra, and L. Pedulli, 1994: Northern and Southern Hemisphere seasonal variability of blocking frequency and predictability. *Mon. Wea. Rev.*, **122**, 1971–2003, https://doi.org/10.1175/1520-0493(1994)122<1971:NASHSV>2.0.CO;2.

Tuel, A., and O. Martius, 2021: A global perspective on the sub-seasonal clustering of precipitation extremes. *Wea. Climate Extremes*, **33**, 100348, https://doi.org/10.1016/j.wace.2021.100348.

Villarini, G., J. A. Smith, M. L. Baeck, R. Vitolo, D. B. Stephenson, and W. F. Krajewski, 2011: On the frequency of heavy rainfall for the Midwest of the United States. *J. Hydrol.*, **400**, 103–120, https://doi.org/10.1016/j.jhydrol.2011.01.027.

Vitolo, R., D. B. Stephenson, I. M. Cook, and K. Mitchell-Wallace, 2009: Serial clustering of intense European storms. *Meteor. Z.*, **18**, 411–424, https://doi.org/10.1127/0941-2948/2009/0393.

Wernli, H., and C. Schwierz, 2006: Surface cyclones in the ERA-40 dataset (1958–2001). Part I: Novel identification method and global climatology. *J. Atmos. Sci.*, **63**, 2486–2507, https://doi.org/10.1175/JAS3766.1.

Wilks, D. S., 2016: "The stippling shows statistically significant grid points": How research results are routinely overstated and overinterpreted, and what to do about it. *Bull. Amer. Meteor. Soc.*, **97**, 2263–2273, https://doi.org/10.1175/BAMS-D-15-00267.1.

Winschall, A., H. Sodemann, S. Pfahl, and H. Wernli, 2014: How important is intensified evaporation for Mediterranean precipitation extremes? *J. Geophys. Res. Atmos.*, **119**, 5240–5256, https://doi.org/10.1002/2013JD021175.

Wolf, G., D. J. Brayshaw, N. P. Klingaman, and A. Czaja, 2018: Quasi-stationary waves and their impact on European weather and extreme events. *Quart. J. Roy. Meteor. Soc.*, **144**, 2431–2448, https://doi.org/10.1002/qj.3310.

Woollings, T., A. Hannachi, and B. Hoskins, 2010: Variability of the North Atlantic eddy-driven jet stream. *Quart. J. Roy. Meteor. Soc.*, **136**, 856–868, https://doi.org/10.1002/qj.625.

Yang, Z., and G. Villarini, 2019: Examining the capability of reanalyses in capturing the temporal clustering of heavy precipitation across Europe. *Climate Dyn.*, **53**, 1845–1857, https://doi.org/10.1007/s00382-019-04742-z.

Yao, Y., and L. De-Hai, 2014: The anomalous European climates linked to different Euro-Atlantic blocking. *Atmos. Oceanic Sci. Lett.*, **7**, 309–313, https://doi.org/10.1080/16742834.2014.11447181.

Zscheischler, J., and Coauthors, 2020: A typology of compound weather and climate events. *Nat. Rev. Earth Environ.*, **1**, 333–347, https://doi.org/10.1038/s43017-020-0060-z.